ACS APPLIED POLYMER MATERIALS

pubs.acs.org/acsapm Article

Tailored Mesoporous Microspheres by Polymerization-Induced Microphase Separation in Suspension

Colin H. Peterson, Jay R. Werber, Hyung Kae Lee, and Marc A. Hillmyer*

Cite This: ACS Appl. Polym. Mater. 2022, 4, 4219−4233 Read Online

ACCESS | Metrics & More | Article Recommendations | Supporting Information

ABSTRACT: We describe the preparation of block polymer beads by aqueous suspension polymerization to create poly(caprolactone) (PCL)-*block*-poly(styrene-*co*-divinylbenzene) beads that can be selectively etched under basic conditions to yield mesoporous polymer microspheres with uniform pore size. Polyvinylalcohol was used to stabilize the suspension polymerization in which styrene and divinylbenzene monomers were polymerized from a PCL macrochain transfer agent (macroCTA). The resulting polymerization-induced microphase separation process led to a nanostructured bicontinuous morphology. The particle size and pore size were independently tunable: the particle size was controlled by the stir rate of the suspension polymerization—yielding average diameters ranging from 60 to 300 μm—while the pore size was determined by the molar mass of the PCL block, with the mode pore diameters being 6 nm and 11 nm after etching beads made using 13 and 45 kg/mol PCL blocks, respectively. Based on nitrogen sorption measurements, the surface areas of the beads were ∼300 m^2/g when using a PCL macroCTA of 13 kg/mol. The beads were homogenous throughout on the micron length scale as determined by confocal Raman microscopy and lacked an impermeable skin layer as confirmed by scanning electron microscopy. Furthermore, the scalability of suspension polymerization allows for the simple synthesis of large quantities of thermoset microspheres with uniform pore size. We also demonstrate the ability to incorporate functional pore walls into the beads using multiblock precursor polymers. These functionalized mesoporous polymer beads show high affinity for ionic dyes in aqueous solutions (as a proof of principle) and remove dye from the solution at rates exceeding those of commercial ion-exchange resins. The developed procedure could be used to generate other functional surface chemistries with important applications in heterogeneous catalysis, chromatography, and water remediation.

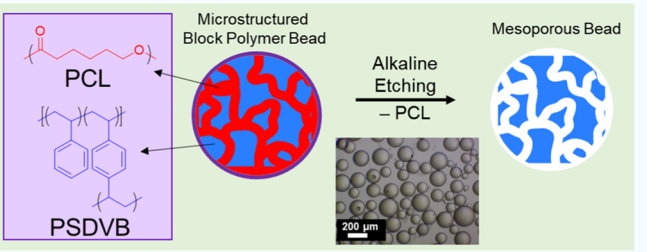

KEYWORDS: *Ion exchange, polymer microspheres, block polymers, mesoporous materials, suspension polymerization, controlled radical polymerization*

INTRODUCTION

Porous polymer microspheres of varied size, composition, functionality, and porosity remain an active area of research due to their wide applicability and tunable properties that can be provided by advances in polymer synthesis.[1−3] Important applications include heterogeneous catalysis—for which sulfonated[4] and dimethylaminopyridine (DMAP)-containing resins have found success—and industrial and analytical separations such as in adsorption and chromatography technologies.[5−8] Suspension polymerization is the dominant technique to prepare relatively large porous polymer beads, with diameters ranging from 20 μm up to the millimeter range.[2] Particles in this size range are of interest in high-flow resin beds and for polymer-supported catalysts.

Porosity is typically introduced in these materials by hypercross-linking or by the inclusion of a porogen during bead formation. Porogens are used in syneresis processes in which the porogen phase separates from the polymer phase during polymerization and is subsequently extracted. These syneresis processes are typically cross-link-induced or interaction-induced (χ-induced, where χ is the Flory−Huggins interaction parameter).[9] An example of χ-induced syneresis is polymerization-induced phase separation, in which the initial reactants are miscible with the porogen, whereas the product polymer is not, and phase separation occurs prior to gelation.[2] Systematic studies on the introduction of small molecule and oligomeric porogens have been reported.[10] In the case where the porogen is compatible with the monomer but incompatible with the polymer, phase separation occurs early in the polymerization process, leading to large voids on the order of hundreds of nanometers to micrometers.[11−13] Although the

Received: February 2, 2022
Accepted: April 28, 2022
Published: May 17, 2022

https://doi.org/10.1021/acsapm.2c00210
ACS Appl. Polym. Mater. 2022, 4, 4219−4233

range of pore sizes obtained can be shifted using this method, the pore-size distribution is always broad. When the compatibility between the polymer and porogen is higher, phase separation occurs later in the polymerization and smaller pore sizes into the micropore regime (<2 nm in diameter) are formed through cross-link-induced syneresis. Mesoporous materials—which contain pore diameters between 2 and 50 nm and are particularly relevant for macromolecule and protein separations—often require more complex formulations of different small molecule or macromolecular porogens.[14] For example, Malik et al. reported the synthesis of mesoporous cross-linked polystyrene (PS) beads where the porogens were mixtures of toluene, naphthalene, and undecane, resulting in sub-10 nm pores.[15] However, as with other syneresis processes, pore-size distributions in this mesoporous regime are necessarily broad, which can limit performance in applications such as chromatography.

In contrast to conventional approaches using porogens, block copolymers are well-suited for forming mesoporous materials—with the added benefit of narrow pore-size distributions. Block copolymers can inherently order into a variety of equilibrium structures with domain spacings on the nanometer length scale that are largely dictated by the polymer molar mass.[16] Selective etching by, for example, hydrolysis,[17] ozonolysis,[18] or ultraviolet (UV) photolysis[19] of one block in these nanostructured systems can give mesoporous materials with narrow pore-size distributions. However, while the tunability and uniformity of pore sizes from block copolymers is advantageous, pore continuity in such ordered systems is often a challenge.[20] Without post-processing, cylindrical morphologies typically have grain boundaries that disrupt pore continuity; challenging and time-consuming pore-aligning techniques are often needed to enable effective mass transport.[21,22] The intrinsically bicontinuous gyroid phase enables pore continuity but typically occupies narrow regions of the morphology map, resulting in synthetic challenges.[23] Additional progress in this area has been accomplished by self-assembly processes including polymer cubosomes[24] and polymerization-induced self-assembly.[25−28] These methods rely on the thermodynamically stable self-assembly of amphiphilic block copolymers to form polymer particles with diameters ranging from hundreds of nanometers to tens of microns. Although these are very well-defined materials, the small particle size requires centrifugation to remove particles from the solution in the context of nanoreactors and catalysis.[29] In addition, both processes require initially amphiphilic block polymers to self-assemble in aqueous systems, which requires specialized syntheses to accommodate disparities in solubility between the different polymer blocks and monomer precursors.

Our group has recently demonstrated that the disordered morphology offers great promise for the generation of continuous pores of uniform size.[30,31] One such method to access the disordered state is polymerization-induced microphase separation (PIMS), in which the composition fluctuations of a weakly segregated block copolymer mixture are kinetically trapped by cross-linking to yield a percolating bicontinuous structure.[30] The length scale of these composition fluctuations are on the order of the radius of gyration[32] of the polymer, whereas in χ-induced syneresis the length scale of macrophase separation ranges from hundreds of nanometers to the micron range. PIMS is typically conducted as reversible addition/fragmentation chain-transfer (RAFT) polymerization with the use of a selectively etchable polymeric macroCTA, which allows for the creation of porous materials after the removal of the sacrificial block.

In laboratory-scale studies, PIMS has most commonly been employed in the bulk systems to yield cross-linked, mesoporous polymer monoliths.[33,34] Although advantageous in some circumstances, scale-up of this bulk method can be hindered by heat-transfer issues, long reaction times for styrenic materials, and the inability to recover and reshape the final material. Multiphase polymerization methods in aqueous media offer great potential to circumvent these challenges while allowing access to desirable microsphere morphologies. For example, Oh et al. recently developed hollow microspheres with a mesoporous shell using a double-emulsion template and microfluidics, in which the PIMS reaction occurs in the oil phase of a water-in-oil-in-water emulsion.[35] Similarly, Werner et al. used pre-formed block copolymers that self-assembled in a double emulsion to obtain porous shells.[36] In both of these cases, the results were spherical shells rather than the homogeneous porous particles that are relevant for applications such as chromatography. Additionally, the microfluidic methods used can be challenging for large-scale production.

We describe the preparation of homogeneous porous microspheres with uniform pore sizes derived from a poly(caprolactone)-*block*-poly(styrene-*co*-divinylbenzene) (PCL-PSDVB)-cross-linked block polymer prepared by scalable suspension polymerization methods. PCL is susceptible to alkaline hydrolysis, allowing for the voiding of PCL domains to afford porous materials. Using small-angle X-ray scattering (SAXS), scanning electron microscopy (SEM), and nitrogen porosimetry, we show that the microsphere formation is independent of diblock polymer nanostructuring. As a result, we obtained in a good yield (>60%) and at a large scale (∼20 g) microstructured polymer beads that could be subjected to alkaline etching to give mesoporous particles with diameters ranging from 60 to 200 μm. Nitrogen sorption measurements of the porous beads determined their surface areas to be up to 300 m^2/g, with pore diameter distributions in the range of 4−20 nm. The pore size and particle size could be tuned independently by changing the molar mass of the PCL macroCTA and the stir rate of the polymerization, respectively. The control over these parameters demonstrates the applicability of diblock microphase separation to the formation of precision porous particles. In addition, we demonstrate the ability to include a functionalizable polymer block between the sacrificial PCL domain and the structural PSDVB domain. By straightforward post-polymerization reactions, we incorporated ionic functional groups along the pore walls. By combining precision pore sizes with tunable functional groups, we show the rapid uptake of oppositely charged dye species from aqueous solutions with capacities that rival commercially available ion-exchange resins with a faster kinetic profile.

MATERIALS AND METHODS

Materials. All chemicals were purchased from commercial suppliers and used as received unless otherwise noted. ε-Caprolactone was purchased from Sigma-Aldrich and purified by vacuum distillation from calcium hydride (Sigma-Aldrich). Styrene, divinylbenzene (technical grade), 4-vinylbenzyl chloride (VBC), and *tert*-butyl acrylate were purchased from Sigma-Aldrich and passed through a short column of basic alumina before use. Polyvinylalcohol (PVA) (15−23 kg/mol M_w, 87−89% hydrolyzed) was purchased from Sigma-Aldrich and used without further purification. Diphenylphosphate (DPP) was purchased from Sigma-Aldrich and dried at 40 °C

https://doi.org/10.1021/acsapm.2c00210
ACS Appl. Polym. Mater. 2022, 4, 4219−4233

under a dynamic vacuum for 24 h before use. Ethylene glycol was purchased from Fisher Scientific and passed through basic alumina immediately before use. DMAP (Sigma-Aldrich) was recrystallized from ethyl acetate before use. Diisopropylcarbodiimide (DIC) (Oakland Chemical) was used without further purification.

Instrumentation. Nuclear magnetic resonance (NMR) spectra were obtained in deuterated chloroform ($CDCl_3$) using a 500 MHz Bruker AVANCE III HD. Analyses were performed using MestReNova software. Multi-angle light scattering with size-exclusion chromatography (SEC) chromatograms were obtained in tetrahydrofuran (THF) using an Agilent 1260 Infinity chromatograph equipped with a Wyatt DAWN Heleos II LS detector and a Wyatt OPTILAB T-rEX RI detector. Samples were evaluated at a concentration of 1 mg/mL in THF, and a literature d*n*/d*c* value of 0.0715 mL/g was used for PCL homopolymers.[37,38] Attenuated total reflection−Fourier transform infrared (ATR-FTIR) spectra were obtained using a Bruker Alpha-P Platinum FTIR. Solid samples were pressed onto the diamond crystal using a manual probe tip. SEM images were obtained using a Hitachi SU8230 field emission gun scanning electron microscope. SEM energy-dispersive X-ray spectroscopy (SEM-EDS) was performed on a Hitachi SU8230 field emission gun instrument with a Thermo Noran System 7 EDS. All the samples were coated with 2 nm of Pt for this analysis. Cross sections of beads were obtained by cryofracturing samples of beads in liquid nitrogen or by cryomicrotomography, where specified. Raman microscopy was performed using a Witec Alpha 300R confocal Raman microscope with a UHTS300 spectrometer and a DV401 CCD detector. A frequency doubled Nd:YAG 532 nm laser was used as the excitation source. SAXS patterns were obtained on a Xenocs Ganesha LabSAXS instrument. Nitrogen isotherms for porosimetry data were obtained using a Quantachrome autosorb iQ gas sorption analyzer. Approximately 50 mg of the dried sample were loaded into 9 mm stems with a bulb and outgassed for 20 h at room temperature before data collection. The Brunauer−Emmett−Teller (BET) and quenched solid density functional theory (QSDFT) analyses were performed using ASIQwin software. The BET analysis was performed using P/P_0 values between 0.05 and 0.35 on the adsorption branch. The QSDFT analysis was performed on the entire adsorption branch using nitrogen on a carbon model assuming cylindrical pores. The dynamic viscosity of polymer solutions was estimated using a Brookfield LVDV-E viscometer utilizing the small sample adapter.

Synthesis of 2-hydroxyethyl-2-(Dodecylthiocarbonothioylthio)-2-methylpropanoate. 2-(Dodecylthiocarbonothioylthio)-2-methylpropionic acid (DDMAT) was esterified with ethylene glycol to provide a primary alcohol to serve as an initiator for the ring-opening polymerization of caprolactone. DDMAT was prepared by a previously reported procedure.[39] A ^{1}H NMR spectrum is shown in Figure S1. 2-Hydroxyethyl 2-(((dodecylthio)carbonothioyl)thio)-2-methylpropanoate (DDMAT-OH) was prepared following a previously reported procedure.[40] In a dry 1 L sidearm round-bottom flask, DDMAT (16.5 g, 45 mmol, 1 equiv) and DMAP (0.5 g, 4 mmol, 0.09 equiv) were dissolved in dichloromethane (DCM) (200 mL). Under positive argon pressure, DIC (50 mL, 0.32 mol, 7.1 equiv) was added to the DCM solution, which became hazy. The solution was allowed to stir at room temperature for 15 min before the addition of ethylene glycol (200 mL, 3.6 mol, 80 equiv). After the addition of ethylene glycol, the reaction was allowed to stir at room temperature for 46 h. The reaction solution was washed with water (150 mL), an aqueous solution of copper(II) sulfate (0.06 M, 200 mL) to remove excess DMAP, saturated sodium bicarbonate solution (2 × 150 mL), and finally brine (150 mL). The organic phase was dried over magnesium sulfate and the solvent was removed by rotary evaporation. The product was purified by column chromatography on silica using a hexanes/ethyl acetate mobile phase followed by rotary evaporation to yield a yellow-orange oil (11 g, 60% yield). 1H NMR (500 MHz, CDCl3): δ 4.32−4.22 (m, 2H), 3.83 (tt, J = 6.2, 3.6 Hz, 2H), 3.35−3.21 (m, 2H), 1.88 (t, J = 6.4 Hz, 1H), 1.71−1.63 (m, 2H), 1.40 (td, J = 11.6, 9.5, 4.4 Hz, 2H), 1.36−1.21 (m, 16H), 0.90 (t, J = 6.9 Hz, 3H). The ^{1}H NMR spectrum is shown in Figure S2.

Synthesis of PCL macroCTA. In a typical polymerization, ε-caprolactone (111.2 g, 0.975 mol, 97 equivalents) was added to an oven-dried 250 mL sidearm flask charged with a magnetic stir bar. The concentrated solutions of DDMAT-OH (4.12 g, 0.010 mol, 1 equivalent) and DPP (5.06 g, 0.20 mol, 2 equiv) in toluene were injected through the septum of the sidearm flask. The flask was then placed into an oil bath set at 60 °C until the stir bar stopped (after 1 h) due to high viscosity, indicating high conversion. The bulk reaction solution was then diluted with an equal volume of chloroform. The reaction was then quenched with 1 mL of pyridine at room temperature. The polymer solution was sampled after quenching but before purification to determine the conversion of caprolactone by ^{1}H NMR spectroscopy, which was determined to be 98%. The rest of the solution was precipitated into methanol, redissolved in THF, and then reprecipitated into hexanes. Dry nitrogen was blown over the polymer before drying in a vacuum oven at 30 °C overnight. PCL was recovered as a yellow powdery solid (106 g, 95% yield, $M_{n,NMR}$ = 13 kg/mol, $M_{n,SEC}$ = 13 kg/mol, $M_{w,SEC}$ = 14 kg/mol, Đ = 1.07). 1H NMR (500 MHz, CDCl3) δ 4.07 (t, J = 6.8 Hz, 231H), 3.66 (t, J = 6.5 Hz, 2H), 3.28 (t, 2H), 2.32 (t, J = 7.6 Hz, 233H), 1.66 (ddt, J = 11.3, 6.8, 2.9 Hz, 479H), 1.45−1.33 (m, 233H), 0.89 (t, 3H). A representative ^{1}H NMR spectrum is shown in Figure S3, and the THF SEC chromatograms are shown in Figures S5 and S6. The characterization data for the two molar masses of the polymer are available in Table S1.

Synthesis of PCL Diblock MacroCTAs. *Poly(caprolactone)-block-polyvinylbenzylchloride.* A PCL macroCTA (5 g, 3.33 × 10^{-4} mol, 1 equiv) was added to a 50 mL round-bottom flask. 4-VBC (13.7 g, 90 mmol, 270 equiv) was added and the solution was homogenized by vigorous vortex mixing. A stir bar and an azobisisobutyronitrile (AIBN) initiator (16 mg, 0.10 mmol, 0.3 equiv) were added. This solution was degassed by bubbling with dry nitrogen for 5 min. The reaction was then heated at 80 °C for 90 min and then 100 °C for an additional 30 min. The polymer was precipitated into methanol, redissolved in THF, and precipitated again into methanol. The purified polymer was then dried overnight in a vacuum oven at 40 °C and recovered as a yellowish solid. The conversion of 4-vinylbenzyl chloride (VBC) monomer was determined by ^{1}H NMR to be 28%, and the yield of the polymer based on this conversion was 89%. The molar mass of the PVBC block was determined by ^{1}H NMR to be 11 kg/mol and by light scattering-SEC (LS-SEC) (Figure S7, left), the number average molecular weight of the block polymer was determined to be 25 kg/mol with a dispersity of 1.21.

Polycaprolactone-block-poly-tert-butylacrylate. A PCL macroCTA (10 g, 6.67 × 10^{-4} mol, 1 equiv) was added to a 100 mL round-bottom flask and dissolved in toluene (15 mL). *Tert*-butyl acrylate (18.5 g, 145 mmol, 216 eq.) was added to the mixture along with AIBN (33 mg, 0.20 mmol, 0.3 equiv). The homogenous solution was degassed by bubbling with dry nitrogen for 5 min. The solution was heated to 80 °C for 40 min, after which it was quenched in ice water and the polymer precipitated in hexanes. The resulting yellow polymer was dried in the vacuum oven overnight at 40 °C. The conversion of the *tert*-butyl acrylate monomer was determined by ^{1}H NMR to be 86%, and the total yield of the polymer was 80%. The molar mass of the poly-*tert*-butylacrylate block was determined by ^{1}H NMR to be 24 kg/mol and by LS-SEC the number average molecular weight of the block polymer was determined to be 28 kg/mol with a molar mass dispersity of 1.37 (Figure S7, right).

Synthesis of PCL-PSDVB Beads. In a typical suspension polymerization, a 500 mL ChemGlass Morton style baffled reactor vessel (CG-1922-01) was charged with 500 mL of 0.5 M NaCl (aq.) and 2.2 g of PVA. The reactor lid (CG-1940-01) was fitted to the reactor body with the three-blade glass stirring shaft (CG-2079-A-01) attached to a Heidolph overhead stirrer. A heating mantle was added under the reactor body and insulated with glass wool and aluminum foil. The temperature of the heating mantle was controlled using an Omega CN76000 temperature controller and a digital thermocouple. The reactor was brought to 60 °C while stirring at 200 rpm to dissolve the PVA. The reactor was then cooled to room temperature and purged with nitrogen gas. In a separate vial, 6 g of PCL-CTA was

https://doi.org/10.1021/acsapm.2c00210
ACS Appl. Polym. Mater. 2022, 4, 4219−4233

Table 1. Preparation and Characterization Data for Samples in This Study[a]

entry	stir rate (rpm)	macroCTA (kg/mol)	DVB[b] (%)	PVA (g/L)	Rxn time (h)	mass yield[c] (%)	PCL content[d] (wt %)	particle size	
								mean diameter (μm)	coefficient of variation
1	500	N/A	33	4	2.5	84	0	61	0.25
2	200	PCL-13k	33	4.4	21	70	40	274	0.45
3	350	PCL-13k	33	2.2	19.5	82	34	138	0.24
4	350	PCL-13k	33	4.4	20	65	43	122	0.35
5	350	PCL-13k	10	2.2	21.5	51	45	105	0.28
6	350	PCL-13k	67	2.2	20	80	30	115	0.37
7[e]	500	PCL-13k	33	4.4	22.5	75	38	67	0.31
8	350	PCL-45k	33	2.2	19.5	59	48	340[f]	[f]
9	350	PCL-45k	33	4.4	21	62	46	370	0.28
10	500	PCL-45k	33	2.2	20	53	53	260	0.2
11	500	PCL-PVBC	33	2.2	20.5	60	27	87	0.28
12	500	PCL-PTBA	33	2.2	19.5	90	10	73	0.39

[a]All the reactions used a 0.5 M NaCl (aq.) solution as the continuous phase and were conducted at 90 °C. The ratio of the combined oil phase (macroCTA, styrene, divinylbenzene, and toluene) to the aqueous phase was kept constant at 4% (w/v) or 20 g of the oil phase to 500 mL of aqueous sodium chloride. [b]Mole percentage divinylbenzene in the monomer solution. [c]Mass yield is calculated by dividing the recovered mass by the theoretical yield, assuming 100% conversion of styrene and divinylbenzene. [d]Determined gravimetrically from the difference in the polymer mass before and after the suspension polymerization. Initially, all the polymer is PCL, which is shown to be quantitatively recovered after the reaction. After polymerization, any mass change is presumed to be entirely from the polymerized styrene and divinylbenzene monomers. Therefore, the PCL content is the initial mass of PCL divided by the dry mass yield of polymer beads. [e]Polymerization conducted at 95 °C instead of 90 °C. [f]Entry 8 was primarily aggregates of spheres with this approximate diameter. As such, the coefficient of variation was not determined.

dissolved in 14 g of a styrene:divinylbenzene solution of a molar ratio of 2:1. Lauroyl peroxide (44 mg, 0.11 mmol) and toluene (2 mL) were added to this solution, which was then bubbled with dry nitrogen gas for 5 min and then added using a syringe to the reactor. The stir rate and temperature were then set according to the experiment (see Table 1) and allowed to react for 20 h. The heating mantle was removed, and the reaction was allowed to cool while stirring. Yellow polymer beads were filtered on a glass frit and washed several times with methanol and water before drying under a vacuum at room temperature for 18 h. After drying, beads were adhered to microscope slides with double-sided tape and magnified images were taken (Figures S11 and S12). The diameters of at least 180 beads were measured by image analysis using ImageJ software to determine the average diameter and the distribution of the mean.

Etching of PCL-PSDVB Beads. Bead samples were etched in 15 mL centrifuge tubes. Beads were added to the tubes before adding 5 mL of methanol and 5 mL of the 3 M NaOH (aq.) base for a final concentration of 6.7% (w/w) NaOH. Sealed centrifuge tubes were gently mixed on an orbital shaker table for 72 h, after which the beads were allowed to settle out of the solution. The etching solution was carefully removed by pipet and replaced with fresh methanol (10 mL × 3). Washed and etched beads were dried under a gentle nitrogen flow and then dried in a vacuum overnight (18 h).

Synthesis of PCL-PX-PSDVB Beads. Beads prepared from the PCL diblock macroCTA [PCL-*block*-poly(*tert*-butyl acrylate) (PCL-PTBA) or PCL-P4VBC] were prepared identically to the PCL-PSDVB beads described above except for the use of 6 g of the diblock macroCTA in place of the PCL homopolymer macroCTA.

Functionalization of Triblock Beads. *Cationic Beads.* Previously dried PCL-P4VBC-PSDVB beads (500 mg) were added to a round-bottom flask (20 mL) charged with a stir bar. Triethylamine (10 mL) and deionized water (10 mL) were added. The sealed flask was placed in an oil bath at 45 °C for 18 h. The beads were then filtered off using a Buchner funnel. The beads were washed with water and methanol, dried under a stream of nitrogen, and then dried under a dynamic vacuum for 18 h at room temperature.

Beads were also exposed to anhydrous triethylamine (10 mL) at room temperature for 18 h. Under these conditions, the PCL domains were not hydrolyzed. These beads were isolated and dried similarly to those exposed to triethylamine/water.

Anionic Beads. Previously dried PCL-PTBA-PSDVB beads (500 mg) were added to a 20 mL scintillation vial. Methanol (7.5 mL) and 3 M NaOH (aq., 7.5 mL) were added. The sealed vial was placed on an orbital shaker table for 42 h. The beads were then filtered by gravity filtration and washed with excess methanol, dried under a nitrogen flow, and dried under a dynamic vacuum for 18 h at room temperature.

The resulting PTBA-PSDVB beads (200 mg) were then deprotected by suspending them in a solution of hexafluoroisopropanol (HFIP, 10 mL) and hydrochloric acid (0.5 mL, concentrated). After 3 h, the solution was poured into a beaker where it was neutralized with aqueous sodium hydroxide. The beads were then filtered and washed with excess water and methanol, dried under a nitrogen flow, and dried under a dynamic vacuum for 18 h at room temperature.

Dye Sorption Studies. The solutions of methyl red (MR), methyl orange (MO), or toluidine blue (TB) were prepared gravimetrically in phosphate-buffered saline (pH = 7.4) and their concentration was confirmed by UV−visible (UV−vis) spectroscopy. For capacity and kinetic measurements, dry beads (40−110 mg) were added to a scintillation vial. A dye solution (15 mL) was added, and aliquots were taken at specific time intervals. Aliquots were diluted by a known factor to result in solutions with an absorbance of less than 1.5 when possible. For column tests, dry beads were added to a glass pipet (5 3/4″) that had been plugged with glass wool. Water or phosphate buffer was run through the column to pre-treat the beads, then dye solution was run through the mini column either with or without applied pressure where noted. Applied pressure was provided manually by a pipet bulb. Kinetics were also conducted by placing cationic beads (11, 15 mg) into a cuvette with the MO solution (3 mL, 1.2×10^{-4} M). The absorbance of the dye solution was monitored every second and recorded until the absorbance plateaued. The sample was then agitated by stirring with a glass rod, which caused the absorbance to continue to decrease.

RESULTS AND DISCUSSION

Polymer Synthesis. We used PCL as the sacrificial block in our suspension PIMS systems due to the ready availability of the monomer, its amenability to ring-opening transesterification polymerization (ROTEP) from an alcohol initiator, and the ability to degrade the resulting polymer under alkaline conditions. PCL is semicrystalline with a glass transition temperature of −30 °C, whereas the polylactide (PLA) used in

https://doi.org/10.1021/acsapm.2c00210
ACS Appl. Polym. Mater. 2022, 4, 4219−4233

previous PIMS studies is amorphous with a glass transition temperature of around 55 °C. Although at the temperature of the polymerization reaction, both PCL and amorphous PLA are polymer liquids, once cooled to room temperature, PCL can crystallize. The effects of crystallization on the microstructure obtained by PIMS were of interest. Both are susceptible to hydrolytic degradation under similar conditions. We prepared the PCL block under water-free conditions using DPP as an acid catalyst.[41] The orthogonal preparation of the first block by ROTEP and subsequent chain extension by RAFT allows for high blocking efficiency. Styrene/divinylbenzene (SDVB) was chosen to be the structural component due to the high glass transition temperature of the resulting cross-linked PS. Additionally, each of the polymer blocks would have distinguishing spectral features to aid in characterization. The characterization details of the initial polymeric CTAs can be found in Table S1 in the Supporting Information.

Suspension Polymerizations. Several control polymerizations were performed to confirm the stability of the components and the amenability of the RAFT process to the suspension conditions. As a baseline for further comparison, a mixture of styrene, divinylbenzene, and lauroyl peroxide without the macroCTA was heated to 90 °C at a stir rate of 500 rpm (Table 1, entry 1). The resulting PSDVB beads had an average (μ) diameter of 61 μm and a coefficient of variation (a ratio of the standard deviation σ to the mean μ) of 0.25 (Figure S10).

Because PCL hydrolyzes under alkaline conditions at room temperature, a sample of PCL was dissolved in toluene and dispersed in water to determine if such degradation would occur under the conditions of the suspension polymerization. After 20 h in the 0.5 M NaCl solution at 90 °C, PCL was recovered quantitatively from the reactor. The SEC trace of the recovered PCL was identical to that of PCL before the hydrolysis test, suggesting that the PCL was not degraded to any appreciable extent on this reaction timescale (Figure S8). Also, NMR analysis indicated negligible loss of the RAFT agent end group (Figure S4). To confirm chain extensibility of the PCL macroCTA, we performed an initial polymerization test with a styrene monomer and no cross-linker. The suspension RAFT polymerization showed high blocking efficiency as the SEC peak shifted to a shorter elution time without apparent residual macroCTA (Figure S9). The multi-angle laser light scattering (MALLS) analysis of the chromatogram suggests that the molar mass increased from 13 to 20 kg/mol, consistent with the 45% conversion of styrene by NMR spectroscopy analysis. Hydrolytic etching of the diblock polymer yielded a styrene homopolymer with a molar mass of 6 kg/mol as measured by SEC, consistent with the observed chain extension of PS.

After determining that the reaction conditions were sufficient for the preparation of block polymer beads by RAFT, we carried out a full-scale test of suspension polymerization using a PCL macroCTA (Scheme 1). The previous literature shows that the incorporation of unreactive macromolecular porogens can affect the particle size distribution and particle shape.[42,43] Additionally, the presence of macromolecular porogens increases the viscosity of the monomer solution. Therefore, if the agitating force required to break up the more viscous PIMS-precursor solution was greater than that of the styrenic monomers, then the higher stir rates and stabilizer concentrations could impede the scalability of the technique. To determine the effect of the macroCTA, a

Scheme 1. Diagram Outlining the Preparation of Mesoporous Beads by Suspension Polymerization[a]

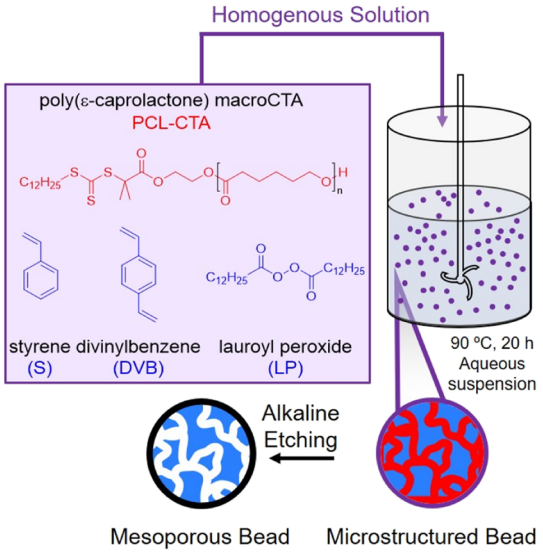

[a](left) Chemical structures of the organic phase components: PCL-CTA, styrene, divinylbenzene, and lauroyl peroxide. (right) The aqueous suspension of the PIMS solution during polymerization, where the insets depict the microstructure of a forming bead before and after basic etching to yield a mesoporous material.

polymerization of a mixture of 30% PCL-CTA and 70% SDVB (Table 1, entry 7) was conducted under otherwise similar conditions to the SDVB control (Table 1, entry 1). Both the SDVB control and the diblock samples exhibited similar average sizes (67 and 61 μm) and particle size distributions as determined by optical microscopy, as shown in Figure 1.

These observations suggest that inclusion of the 13 kg/mol PCL macroCTA did not significantly affect the particle size distribution despite the increased viscosity of the initial solution or the change in the polymerization mechanism from classical free radical to RAFT polymerization. With or without the macroCTA, the only aggregates that formed were on the stir shaft and on the thermocouple; that is, polymer that was not adhered to a surface was recovered as discrete beads, with a range of 60−84% overall yield between multiple runs. The deviation in the total mass content of PCL in the initial polymer−monomer solution (30%) and the final polymer beads (30−53%, Table 1) is most easily explained by the loss of the styrene monomer either to the continuous phase, to the headspace of the reactor, or from evaporation and escape from the reactor. This is reflected in the mass yields below 85% for all the entries in Table 1. Representative optical microscope images of the beads listed in Table 1 are shown in Figures S10−S12.

Characterization of Block Polymer and Etched Beads. We employed an array of spectroscopic, microscopic, and thermal techniques to characterize beads before and after hydrolytic etching. To determine the homogeneity of the spheres on the micron scale, we employed confocal Raman microscopy to obtain composition maps of thinly sliced bead samples prepared by a microtome after being embedded in epoxy resin. Beads were imaged using a confocal microscope, after which a Raman spectrum was collected from every square micron of the 20 μm × 20 μm image. An example Raman spectrum is shown in Figure S20. The relative intensity of

https://doi.org/10.1021/acsapm.2c00210
ACS Appl. Polym. Mater. 2022, 4, 4219−4233

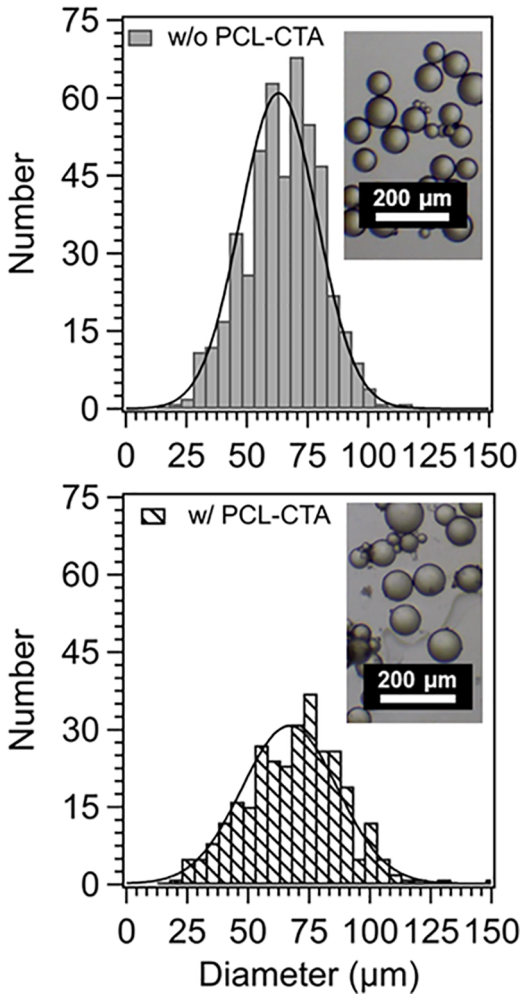

Figure 1. Histograms for entries 1 (top) and 7 (bottom) with a bin width of 5 μm. Samples were prepared under similar conditions, except 7 was prepared with 30% 13 kg/mol PCL-CTA, while entry 1 was performed in the absence of PCL. Solid lines overlaid onto the histograms are gaussian fits to the histogram. 483 beads were counted for entry 1, with an average of 61 μm and a standard deviation of 16 μm. 304 beads were counted for entry 7, with an average of 67 μm and a standard deviation of 21 μm. Insets show representative optical micrographs of the two samples.

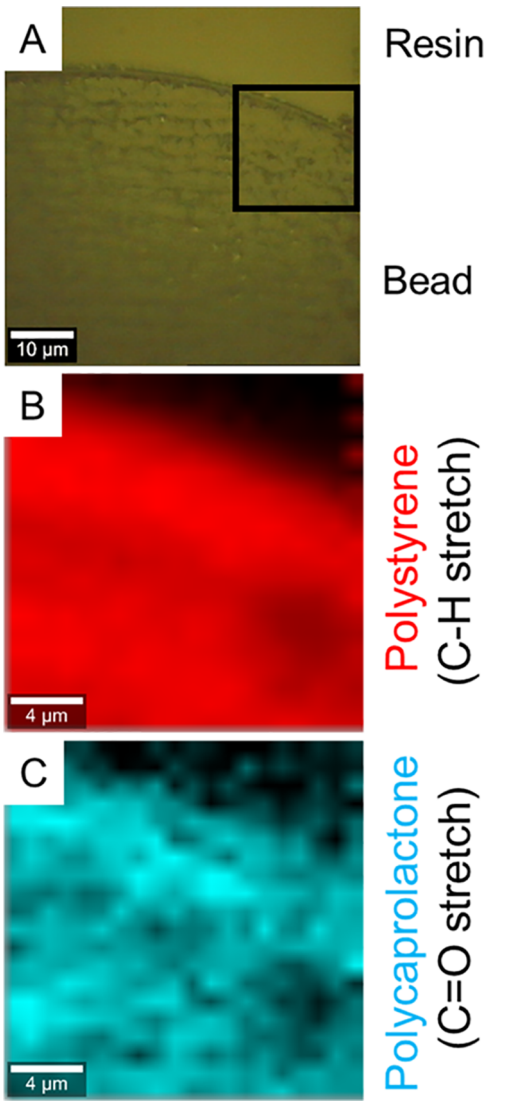

Figure 2. Optical and false color images of a bead from batch 2, derived from the 13 kg/mol PCL macroCTA, prepared by microtome. (A) Optical microscope image of the polymer bead embedded in epoxy resin and sectioned by microtomography. The black border depicts the area used to generate false color images (B,C). (B,C) False color images from scans across the surface of the bead with a resolution of 1 μm^2. (B) Band: 2970−3070 cm^{-1}, corresponding to the aromatic C−H stretch from PS. (C) Band: 1670−1770 cm^{-1}, corresponding to the C═O stretch in PCL. The lower right of both images exhibited a drop in the intensity, possibly due to a defect introduced in the microtome preparation.

peaks corresponding to the carbonyl C═O stretch in PCL (1729 cm^{-1}) or the aromatic C−H stretch in PS (3050 cm^{-1}) were then plotted for each point interrogated (Figure 2).

We expected this PIMS material in these beads to exhibit little composition fluctuation at the micron scale. Therefore, with 1 μm^2 resolution, the presence of PS and PCL was expected to appear uniform. Additionally, the optical transparency of the beads in general suggested few scatterers on these larger length scales. In Figure 3B,C, we can see that the presence of the PCL is qualitatively paired with that of PS. By comparing the gray values of the false color image as a normalized intensity, the ratio of PS to PCL across the surface was typically close to 1 (Figure S21). Also, the average ratio tended to 1 across and down the surface of the microtomed bead, suggesting colocalization of the two domains (Figure S22). Notably, when one signal decreased, the other did as well, suggesting that neither domain existed without the other. The Raman composition maps and transparency of the beads suggest that the polymers were not separated on large length scales (i.e., macrophase separation did not occur) and that the composition of the beads throughout their interior was homogenous).

Beads were submerged in a 6.7% (w/w) solution of NaOH in a 1:1 methanol/water mixture to hydrolyze and remove the PCL, leaving a porous styrenic network. The change in mass after etching agreed well with the expected mass loss associated with the hydrolysis and removal of the PCL domains (Table S2). ATR-IR measurements allowed us to probe the chemical structures present before and after etching the samples. In particular, the carbonyl stretch at 1723 cm^{-1} was used for the PCL domains due to its strength and isolation from other signals. After 72 h of etching, the PCL signals disappeared, strongly suggesting the removal of the PCL domains (Figure

https://doi.org/10.1021/acsapm.2c00210
ACS Appl. Polym. Mater. 2022, 4, 4219−4233

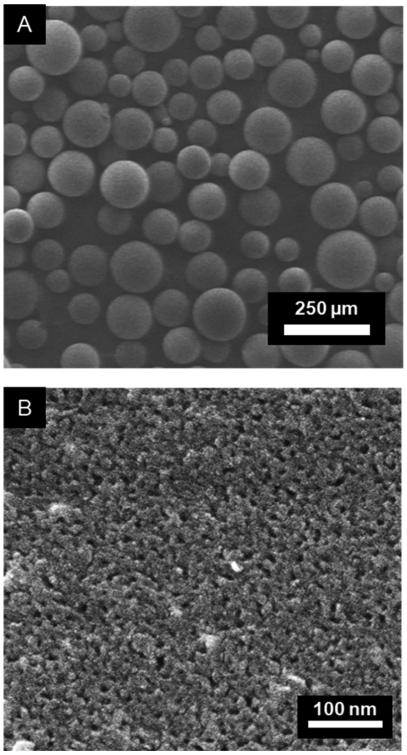

Figure 3. SEM images of beads from batch 3, prepared from the 13 kg/mol PCL macroCTA, after etching in a basic solution. (A) Low magnification view of multiple beads. (B) High magnification view of the surface (light) of a single bead showing nanopores (dark).

S25). However, because the penetration depth for ATR-IR is only ~2 μm, we used complementary thermal techniques to confirm etching throughout the sample.

Differential scanning calorimetry (DSC) was used to monitor the thermal transitions in the polymer bead samples before and after etching. The glass transition of the styrenic domain was apparently elevated far above the usual range, likely due to the extent of cross-linking, and was therefore not visible below the decomposition temperature of the material.[44] We therefore expect to see the thermal transitions associated solely with the PCL domain. Homopolymer PCL has a crystalline melting point at 60 °C and a glass transition at −60 °C as determined by DSC.[45] We observed a weak glass transition signal in both the bulk PCL samples and in the microstructured beads at approximately −58 °C (Figure S28), suggesting little effect on the segmental dynamics of the PCL as compared to the homopolymer in the bead and microphase separation between the styrenic and PCL domains.

We observed a crystalline melting transition with a peak at 56 °C for both the 13 and 45 kg/mol PCL macroCTAs, as determined by the second heating cycle (Figure S28A,B). However, in the microstructured beads, we observed a significant decrease in this melting temperature. For the 13 kg/mol samples, we recorded a reproducible (i.e., persistent through multiple heating cycles) melting temperature at 40 °C for multiple samples of varying particle diameter, suggesting that the dependence is not due to the particle size. The beads prepared from the 45 kg/mol PCL macroCTA had a melting temperature of 50 °C that was consistent across multiple heating cycles. Considering the nanostructured morphology of the PIMS beads, the depression of the melting temperature is likely due to the nanoconfinement of the PCL domain. The melting temperature of crystals including polymer crystallites is in part determined by the dimensions of the crystal. Extensive work on the crystallinity of PCL domains within the PCL-PS copolymer lamellae has been reported by Nakagawa et al.[46,47] In one of their systems, a 45 kg/mol PCL chain tethered on one side to the PS interface exhibited a melting temperature of 50 °C. This is consistent with the 45 kg/mol PCL-derived beads discussed in this work despite the difference in the morphology between the ordered lamellae and disordered bicontinuous domains explored in this work. After hydrolytic etching, the crystalline transition is no longer present, again suggesting the removal of the PCL domain.

SEM was employed to directly image beads before and after etching to confirm the expected morphology and to determine whether a skin layer was formed on the beads (Figure 3B). An undesirable impermeable skin layer would arise if one of the polymer domains had more favorable interactions with the aqueous phase, driving one domain to the oil−water interface. The direct imaging of a bead before etching showed a smooth surface (Figure S16). The etched bead showed a porous structure such as those observed previously in PIMS systems.[30,33,34,44] Additional SEM images are available in the Supporting Information (Figures S12−S17).

SAXS was also employed to confirm microphase separation in bead samples (Figure 4). The features of the SAXS pattern of the mesoporous beads are virtually identical to the pattern obtained from the monolith prepared by PIMS in the bulk (Figure S36), suggesting that the PIMS is not affected by the

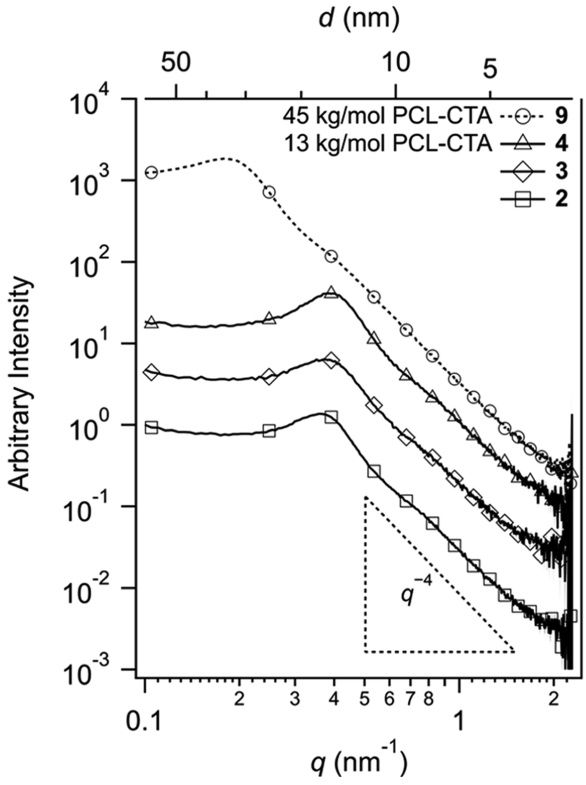

Figure 4. SAXS patterns for PCL-PSDVB PIMS beads after hydrolytic etching to remove the PCL domain. The sample legend refers to table entries in Table 1. Superimposed onto the plot is a line with a slope of −4, which is the expected q dependence for a flat interface from Porod's law.[53] Arbitrary vertical shifts are applied to the curves for clarity.

https://doi.org/10.1021/acsapm.2c00210
ACS Appl. Polym. Mater. 2022, 4, 4219−4233

suspension polymerization conditions. After etching, the high contrast between the voided pores and the styrenic domain allowed for the observation of a broad and well-defined scattering peak. In the 13 kg/mol samples, the maximum of this broad peak appeared at approximately 0.38 nm^{-1}, corresponding to a domain spacing of 17 nm. The samples prepared from the 45 kg/mol PCL-CTA have a domain spacing of 35 nm. This domain spacing corresponds to the average distance from the center of one PSDVB domain to the center of another. The decay region of the scattering pattern gives information about the interface between distinct domains in the system. A perfectly smooth interface is predicted to have a decay that scales with q^{-4}.[48,49] Porous materials with surface roughness at the solid−void interface are predicted to have a decay where this scaling factor is between −3 and −4, with smoother interfaces exhibiting the predicted −4 scaling and weaker scaling for rougher surfaces.[50,51] The scaling behavior of the etched beads was found to vary between −3.4 and −3.6 for samples prepared from the 13 kg/mol PCL macroCTA and around −3.8 for samples prepared from the 45 kg/mol PCL macroCTA. These values suggest surfaces with roughness comparable to other porous materials such as carbon black and charcoal.[52]

Nitrogen sorption isotherms were measured to confirm the porosity, the continuous nature of the pores, and to estimate the specific surface area of the samples. Before etching, the surface area of the beads is limited to the external surface as the pore volume is still occupied by PCL. We can estimate the surface area of a 100-μm diameter PS bead as a smooth sphere to have a specific surface area of approximately 0.06 m^2/g, which is negligible compared to mesoporous samples that can have specific surface areas of several hundreds m^2/g. The sorption isotherms of unetched beads indicate little porosity in the micro- and mesoporous regimes, as expected (Figure 5).

Isotherms for representative etched beads are shown in Figure 5. All the isotherms of etched beads showed low uptake at low pressure (consistent with low microporous content), a high-pressure plateau, and a wide hysteresis loop in the desorption branch indicative of pore-filling behavior. These observations classified these samples as having a type IV isotherm, indicative of mesoporous materials.[54] Performing a BET analysis on the samples yielded surface areas of 260−300 m^2/g for the 13 kg/mol samples. By using a QSDFT model assuming cylindrical pores and a carbon surface, we estimated the pore diameters to be approximately 6 nm. For sample 4, the domain spacing from SAXS was 17 nm and the mode pore diameter was 6.3 nm. The pore volumes for the samples, based on the QSDFT analysis, were around 0.3−0.4 mL/g. If we assume the pore volume is equal to the PCL domain volume before etching, then the measured pore volume would reflect the volume composition of PCL in the beads on a per gram basis. As an example, the pore volume of 4 was found to be 0.38 mL/g by the DFT model. Entry 4 was determined gravimetrically to have a PCL mass content of 43% (w/w) (Table 1). Using the bulk density for semicrystalline PCL (ρ = 1.145 g/mL), the PCL domain would occupy 0.38 mL per gram of cross-linked polymer before hydrolytic etching. Therefore, the expected volume of PCL matches well with the pore volume obtained by etching the cross-linked polymer.

Tunability of Particle and Pore Size. We investigated the effects of the stir rate, surfactant concentration, S:DVB molar feed ratio, and PCL molar mass on the particle size distribution and appearance. The stir rates of 200, 350, and

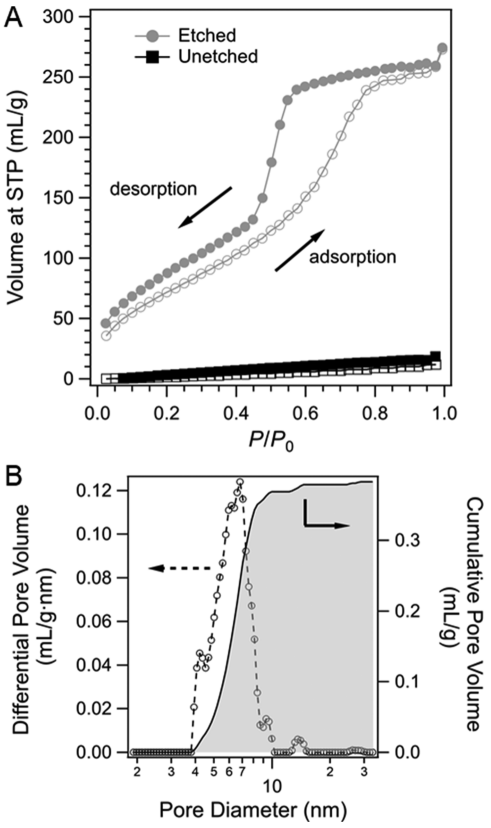

Figure 5. Nitrogen porosimetry data for mesoporous beads (entry 2) prepared from the 13 kg/mol PCL macroCTA. (A) Nitrogen sorption isotherm for bead sample **2** (Table 1). Open symbols show the adsorption branch and filled symbols show the desorption branch. The squares show a sample before etching with negligible porosity. Circles show the etched mesoporous sample. (B) Pore volume from the QSDFT analysis of the nitrogen isotherm. The dashed line shows the differential pore volume and the solid line shows the cumulative pore volume.

500 rpm were chosen at the constant PCL macroCTA (13 kg/mol), concentrations of the stabilizer and cross-linker, the ratio of the PCL macroCTA to the monomer, the ratio of the organic phase to the aqueous phase, and the dimensions of the reactor. Representative optical microscope images for the 13 kg/mol PCL bead series are shown in Figure 6A−C. The width of the particle size distribution decreased as the stir rate increased, but the coefficient of variation (σ/μ) remained in the range of 0.25−0.45. Therefore, the particle size distribution at each stir rate was quite broad when compared to relatively monodisperse particles obtained by methods such as emulsion, dispersion, or seeded polymerization. Hopff et al. reported that the particle size in suspension polymerizations varied with the stir rate to the power of -1.5 ± 0.2.[55] In the present study, the particle size dependence on the stir rate appears to follow a power law with an exponent of −1.2 for samples 2, 4, and 7, as shown in Figure 6. Hinze reported that the maximum droplet size under turbulent flow would follow a power law with an exponent of −1.2, following an analysis of the critical Weber number of dispersed phases.[56] The stir rate dependence observed in this report agrees very well with the Hinze analysis and reasonably well with the Hopff results. One reason for the discrepancy could be the relatively small fraction of the dispersed phase in this work to avoid coalescence, which would more closely align with the assumptions in Hinze's work.

https://doi.org/10.1021/acsapm.2c00210
ACS Appl. Polym. Mater. 2022, 4, 4219−4233

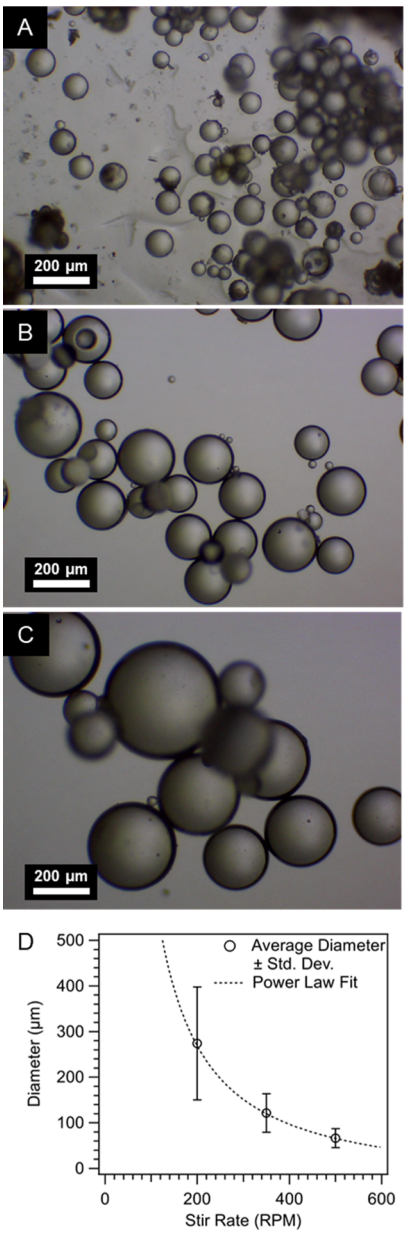

Figure 6. Stir rate dependence of the particle diameter for particles made using the 13 kg/mol PCL-CTA. (A–C) Representative optical microscope images of PIMS beads prepared using 4.4 g/L PVA and stir rates of 500 (A), 350 (B), and 200 rpm (C). (D) Plot of the average diameter versus the stir rate. The error bars represent the standard deviation for each population. The dashed line is a fit of the data to a power law with an exponent of −1.2. The dashed line is an overlay of a power law function with an exponent of −1.2 as predicted by Hinze.[56]

We then explored the role of the divinylbenzene content on the particle morphology, size, and yield. Previous reports have found that higher divinylbenzene content yielded smaller particles with smoother surfaces, as low divinylbenzene content led to insufficient network formation to maintain the particle shape.[57] Using the 13 kg/mol PCL macroCTA and a stir rate of 350 RPM, we varied the amount of cross-linking by changing the feed ratio of styrene and divinylbenzene from 10 to 67% divinylbenzene. The total monomer to macroCTA ratio was held constant (70:30), as was the ratio of the organic phase to the aqueous phase (1:25). Particle size was found to be insensitive to the divinylbenzene content in this system (Figure S35). The role of the cross-linker in maintaining the particle shape may be outweighed by the increased viscosity of the oil phase in our system, which may prevent droplet deformation by increasing the force required to change the shape of the bead.[58] The viscosity of the 13 kg/mol PCL macroCTA (30% w/w) in the monomer solution was >10 000 cP at room temperature, whereas the viscosity of the styrene monomer is 0.695 cP.[59]

When using a 45 kg/mol PCL-CTA, we expected the higher viscosity of the precursor PIMS solution (30% PCL in SDVB) to impede the formation of well-defined spheres. At a stir rate of 350 rpm and a PVA concentration of 2.2 g/L, most of the polymer coalesced to yield large aggregates (see Table 1, entry 8). Spherical particles were observed as both free particles and particles fused to the aggregates. The coalescence of the dispersed phase suggests poor colloidal stability. Microstructured beads were obtained when either the stir rate (Table 1, entry 10) or the stabilizer concentration (Table 1, entry 9) was increased. The average particle diameter as measured by optical microscopy was between 3 and 4 times greater when the 45 kg/mol macroCTA was used compared to the 13 kg/mol macroCTA, for otherwise similar conditions. The pore size of the beads derived from the higher molar mass 45 kg/mol PCL macroCTA (samples 8, 9, and 10) had a mode pore diameter of 10 nm (Figure S33). This demonstrates that the mode of the pore size distribution can be controlled by the molar mass of the macroCTA. The range of pore diameters (5–20 nm) is wider than the range of pore diameters from the 13 kg/mol PCL macroCTA (3–9 nm). The wider range can be attributed to the larger polymer dispersity in the 45 kg/mol precursor than in the 13 kg/mol precursor (Đ = 1.4 and 1.07, respectively). The wider range of pore sizes is a consequence of the wider range of chain lengths present in the precursor. The tunability of pore size based on the macroCTA molar mass described above is independent of the stir-rate-dependent particle size, demonstrating that the present system allows for good control of the particle morphology.

Preparation and Characterization of Wall-Functionalized Particles. Another potential advantage of the present system is the ability to controllably functionalize the pore walls by changing the chemistry of the macroCTA.[60] In particular, we prepared PIMS-formed beads with cationic- and anionic-functionalized pore walls through the suspension polymerization of PSDVB from a diblock macroCTA (PCL-PX-CTA), where PX is a polymer that can be easily modified to obtain the desired (in this case, ionic) functionality. In this way, the functional polymer block is positioned at the interface between the PCL and the cross-linked PSDVB (Scheme 2). After the removal of the PCL and the concomitant introduction of porosity, the PX blocks were modified to yield pore walls that were lined with cationic or anionic polymer chains.

Pre-functional PCL-containing diblocks were prepared as described in the materials section below. The characterization details for the PCL-PX polymers are shown in Table S1. Precationic PCL-PVBC was chosen for its ability to be modified to a quaternary ammonium salt.[61] The molar masses of the PCL block and the PVBC block were 13 and 11 kg/mol, respectively, as determined by ^{1}H NMR spectroscopy. For an anionic system, PCL-PTBA was used as it could be deprotected to acrylic acid after etching to remove PCL. The molar masses of the PCL block and the PTBA block were 13

https://doi.org/10.1021/acsapm.2c00210
ACS Appl. Polym. Mater. 2022, 4, 4219–4233

Scheme 2. Cartoon Depiction of the Triblock PIMS Nanostructure before (Left) and after (Right) the Removal of the PCL Domain (gray) by Hydrolysis[a]

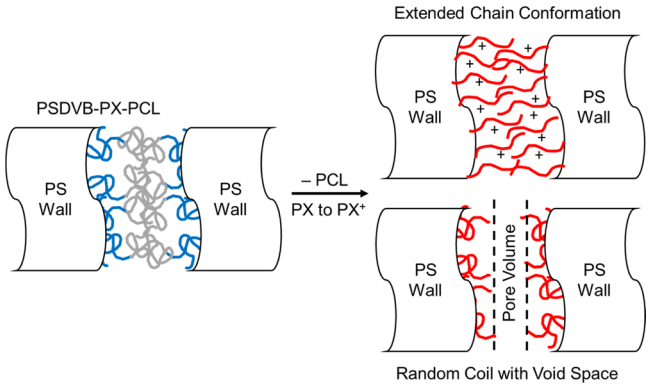

[a]Functionalization is depicted by the color change from blue (neutral precursor) to red (in this example, a positively charged block). Two possible morphologies are described: a charged extended chain conformation with pore filling behavior (top right) and a coil morphology with pore volume (bottom right).

and 24 kg/mol, respectively, as determined by ^{1}H NMR spectroscopy. Both transformations are shown in Scheme 3.

Beads employing either of the diblock polymers were prepared identically to beads prepared from the PCL homopolymer. The total mass ratio of the macroCTA to SDVB was constant (30% macroCTA) as in the homopolymer preparations, meaning that the resulting beads contained less PCL than the homopolymer-derived beads. The total yields of the PCL-PX PIMS beads were within the range of yields obtained from the homopolymer macroCTAs. The average bead diameters for the PCL-PVBC- and PCL-PTBA-derived samples were 87 and 73 μm, respectively. These sizes are more like the beads prepared from the 13 kg/mol PCL macroCTA at 500 RPM (67 μm) than those prepared from the 45 kg/mol macroCTA (260 μm). If the molar mass of the macroCTA was the only determinant of the final bead size at a given stirring power, we would expect the block-derived beads to be much larger.

Pre-cationic beads (entry 11) were simultaneously functionalized and etched with 30% triethylamine in water. The IR spectra (Figure S26) taken before and after etching demonstrate the removal of the PCL by the disappearance of the PCL carbonyl peaks. Functionalization can be seen by the appearance of a C−N stretch at 1220 cm^{-1} and by the disappearance of the terminal alkyl halide C−H stretch at 1295 cm^{-1}. IR after functionalization and washing with water also shows a broad band around 3200 cm^{-1}, which can be attributed to O−H stretches. These stretches may arise from water bound to charged sites or from the hydrolysis of the benzyl chloride group to benzyl alcohol pendant groups. After functionalization, the appearance of a step mass loss of approximately 10% can be seen in the thermogravimetric analysis (TGA) thermogram between 150 and 200 °C in Figure S31. This can be attributed to the thermal degradation of the quaternized ammonium and agrees well with the expected mass loss by the release of triethylamine. Pre-cationic beads exposed to anhydrous triethylamine exhibited no loss of mass. The IR spectra of these beads showed that they still had PCL content. Therefore, the hydrolytic etching requires the presence of water to successfully remove the PCL polymer. These unetched triethylamine-exposed beads were used later as a control sample in dye sorption studies. SEM-EDS elemental mapping images were obtained on cross sections of functionalized beads to demonstrate the inclusion of nitrogen after exposure to triethylamine, either with or without water (Figure S24). Combustion analysis performed on the precursor beads and the functionalized beads showed enrichment of nitrogen content after functionalization, supporting the conclusion that the benzyl chloride groups were transformed to quaternary ammonium salts (Table S3).

The PCL was removed from the pre-anionic beads (entry 12) under alkaline conditions to render them porous, after which they were exposed to a solution of HCl in HFIP to remove the *tert*-butyl group.[62] The polyacrylic acid blocks were then deprotonated in sodium hydroxide prior to character-

Scheme 3. Chemical Schemes for the Removal of PCL and the Conversion of Benzyl Chloride to Benzyltriethylammonium (Left) and the De-*tert*-butyloxylation of *tert*-Butyl Acrylate (Right)

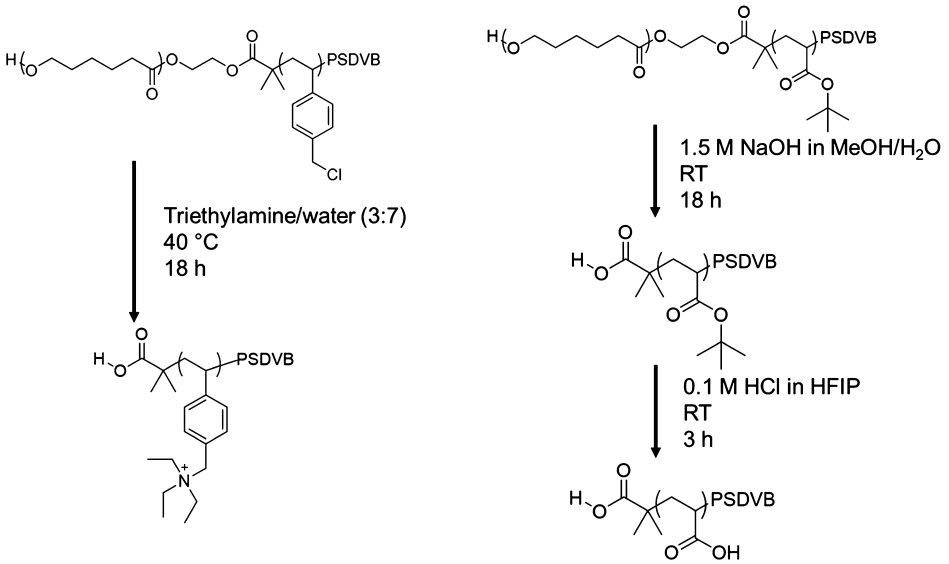

https://doi.org/10.1021/acsapm.2c00210
ACS Appl. Polym. Mater. 2022, 4, 4219−4233

ization. After deprotection, the IR signal of the carboxylate stretch (1574 cm^{-1}) can be seen as opposed to the carbonyl stretch (1724 cm^{-1}) seen before deprotection and deprotonation. The disappearance of all the carbonyl stretches and the appearance of the carboxylate stretch suggests not only complete removal of the PCL but also complete deprotection and deprotonation of the polyacrylic acid (Figure S27). The TGA shows a sharp step mass loss at 250 °C in the pre-anionic beads (entry 12). This is attributed to the thermal release of isobutylene from the polymer (Figure S30). After acidic deprotection, this step mass loss is no longer seen, further supporting the total removal of the *tert*-butyl groups.

The microstructure of these polymer beads was explored by SAXS, nitrogen sorption experiments, and electron microscopy. The domain spacing for the pre-anionic beads appears to be in the range of 40 nm, like those prepared by the 45 kg/mol PCL-CTA (Figure S37). In contrast, the SAXS domain from the pre-cationic beads described was closer to 16 nm, more like those prepared from the 13 kg/mol beads. Nitrogen isotherms were taken to determine the BET surface area and total pore volume of the samples (Figure S34). The anionic beads showed diminished surface area (85 m^2/g) and pore volume (0.29 mL/g) compared to unfunctionalized beads (i.e., 303 m^2/g for sample 2). In part, this may be due to the smaller etchable volume of PCL in these triblock beads relative to the diblock beads. Based on the 10% PCL mass fraction in these beads (compared to 30−50% in the unfunctionalized beads), one would expect roughly 1/3 of the specific surface area based on this alone, which is in general agreement with the observed levels. SEM images (Figure S18) show porosity after the removal of the PCL by alkaline etching.

However, the cationic beads (entry 11) showed negligible pore volume (0.061 mL/g) despite the greater PCL mass fraction. A BET analysis of the nitrogen sorption isotherm resulted in non-physical results for the BET *c* constant, and so a BET surface area could not be calculated. It is possible that the lack of apparent porosity is due to pore collapse stemming from capillary forces during drying. This could occur due to low segregation strength between (uncross-linked) PS and PVBC.[61] The near miscibility of the PS and PVBC blocks may have led to some softening of the pore walls, especially when the beads were dried between each of the functionalization and etching steps. This contrasts with the stronger segregation between PTBA and PS, which led to better defined pores in the anionic beads.[63] However, the size of the cationic beads does not change appreciably on average after functionalization as it might if pore collapse occurred. SAXS scattering (Figure S37) suggests that even after the removal of the PCL block, the system retains a nanostructured morphology which could facilitate mass transport. It is therefore possible that the poly(vinylbenzyl triethylammonium) block adopts an extended chain conformation that fills the pores in the absence of the PCL block. The SEM analysis (Figure S19) shows increased surface roughness after etching, which we interpret as the removal of the PCL domains and void-filling behavior by the charged poly(vinylbenzyl triethylammonium) blocks.

Dye Sorption Studies with Functionalized Beads. Dye sorption was used to confirm the functionalization of the beads. Pre-cationic beads were exposed to aqueous triethylamine as described above to hydrolyze the PCL and quaternize the benzyl chloride groups. In addition to the fully quaternized and PCL-hydrolyzed beads, the dye sorption behavior of as-prepared beads and etched PS-PCL non-ionic beads was also used (entry 7). Cationic beads exposed to anhydrous triethylamine as described above were also used to determine the effect of the intact pore-blocking PCL domains. For this section, the nonfunctional porous beads (entry 7) will be referred to as PIMS-7NF, the as-prepared beads (entry 11) as PIMS-11AP, the beads exposed to *anhydrous* triethylamine to quaternize the benzyl groups as PIMS-11Q, and the beads exposed to aqueous triethylamine to both hydrolyze the PCL domains and quaternize the benzyl groups as PIMS-11HQ. A sample of each of these beads was exposed to identical solutions of pH buffered (pH = 7.4) aqueous solutions of MR dye (3.37×10^{-5} M), a monocarboxylic acid, on an orbital shaker table overnight.

After carefully decanting the solution to remove the beads, the supernatant solution was observed and a UV−vis measurement was taken to determine the concentration of residual dye. The solution from the PIMS-11HQ beads was colorless and the UV−vis measurement showed that >99.7% of the dye was taken up by the beads; the UV−vis absorbance of the residual dye was difficult to distinguish from the baseline absorbance of distilled water. The PIMS-11AP beads took up 2% of the dye in the same time frame, as determined by UV−vis measurements. A low amount of dye sorption was expected as these beads were neither functionalized to allow for ionic interactions between the dye nor were they porous to allow for large surface areas for hydrophobic interactions. The PIMS-11Q beads had taken up 99.3% of the dye. The anhydrous triethylamine was able to permeate into the beads to quaternize the benzyl chloride groups, introducing cationic sites. Therefore, these beads exhibited dye sorption from the solution. The PIMS-7NF beads had taken up 94% of the dye. The sorption of the dye onto the neutral mesoporous beads was attributed to hydrophobic interactions, in keeping with the surface area described in the nitrogen sorption experiments. It is important to note that in this dilute dye solution, the neutral mesoporous beads had already reached their capacity of dye, whereas the cationic beads, whether porous or non-porous, achieved quantitative dye removal.

Following these promising preliminary tests, a further set of studies were conducted using a buffered (pH = 7.4) aqueous solution of MO (a related monocarboxylic acid dye) at higher concentrations (3.05×10^{-3} M) to establish the maximum amount of dye that could be sequestered by the beads. MO was used because its greater solubility in water meant more concentrated solutions could be prepared to test the sorption limits. Amberlite HPR4811 resin was used to compare the performance of the cationic PIMS-11HQ beads to a commercial material as it is also a styrenic resin bearing quaternary ammonium groups. Possibly owing to the nanostructure present in the PIMS-11HQ beads, the dye sorption was extremely fast (Figure 7). 99.8% of the dye was taken up within 15 min of the dry beads being added to the dye solution. In contrast, the PIMS-11Q beads exhibited much slower dye sorption and an apparent induction period in the first 100 s where no dye was taken up from solution. There is a stark contrast in the rate of dye sorption between the PIMS-11HQ beads where the PCL was removed (Figure 7, circles) and the PIMS-11Q beads where the PCL domains were intact (Figure 7, triangles). This suggests that despite the lack of porosity observed from the nitrogen sorption isotherms, there may still be channels through which the dye may travel more rapidly. The Amberlite resin took up 75% of the MO after 180 min. A first-order exponential fit to the Amberlite dye sorption

https://doi.org/10.1021/acsapm.2c00210
ACS Appl. Polym. Mater. 2022, 4, 4219−4233

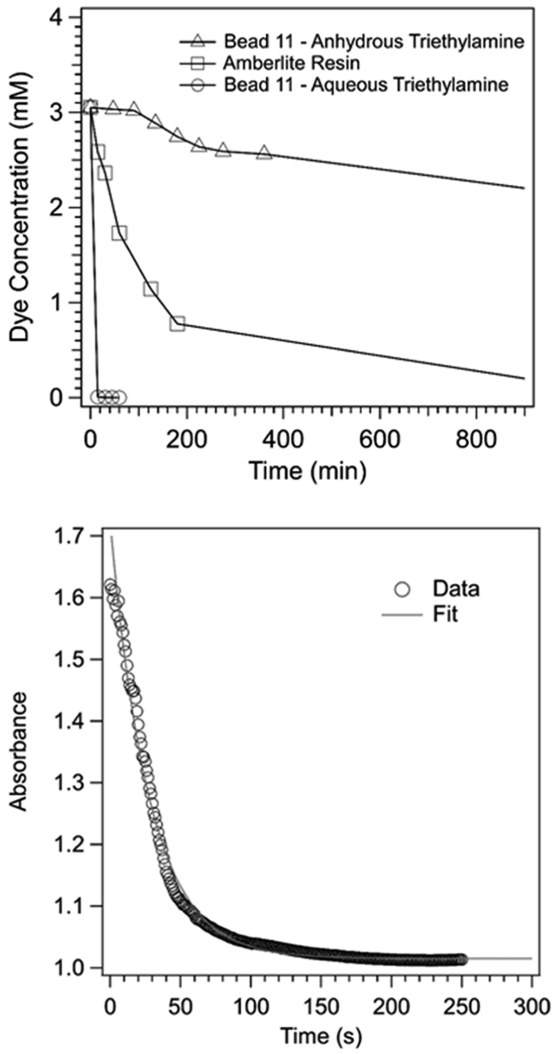

Figure 7. (Top) MO sorption kinetics for PIMS 11-Q beads 11 (triangle) and PIMS-11HQ beads 11 (circle) and commercial Amberlite beads (squares). The lines are drawn between points to guide the eye. (bottom) PIMS-11HQ beads 11 (circles) recorded directly in the spectrometer to facilitate measurement at shorter times along with a single exponential fit.

(not shown) results in a rate constant of 1.4×10^{-4} s^{-1}. The high rate of dye sorption on the PIMS-11HQ beads precluded determination of a rate constant from these data. As at least five half-lives occurred in 15 min, we can estimate that the rate constant in the PIMS-11HQ beads is 2−3 orders of magnitude greater than in the Amberlite resin. A further experiment was performed to support this estimate below.

To estimate the rate constant of dye sorption onto the PIMS-11HQ beads (from entry 11), a dilute solution (3 mL, 1.2×10^{-4} M) was directly monitored in the spectrometer at 462 nm. PIMS-11HQ beads (15 mg) were added and the decay in absorbance was recorded (Figure 7). The solution was not actively stirred or agitated during this process until the absorbance reached a plateau, at which point the solution was agitated with a glass stir rod. Boundary layer issues may also complicate the sorption of the dye from solution in this static absorption study. With these limitations in mind, the rate constant extracted from the exponential fit was 3.6×10^{-2} s^{-1}—250 times greater than that of Amberlite, consistent with the abovementioned estimate. This suggests that despite the lack of porosity visible by nitrogen sorption, there may exist channels through which the dye can access the entirety of the bead rapidly through the cationic domains.

Cationic and anionic beads were also tested in a column format. Approximately 50 mg of beads were loaded into a glass pipet plugged with glass wool. In these tests, 10 mg/L solutions of either MR (for cationic beads) or TB (for anionic beads) were run through the mini column, either with or without added pressure. The absorbance of the dye from the solution was rapid enough that the effluent was colorless and >99% of the dye had been removed from the solution as measured by UV−vis. Dye removal was measured with or without applied pressure supplied by a pipet bulb, and in both cases, removal was >99%, as the residual dye concentration was below the limit of quantification on the UV−vis instrument (Figure S38).

To measure the total dye capacity of the cationic beads, a sample of PIMS-11HQ was placed in a solution of excess MO. The expected capacity of the beads is approximately 405 mg of MO for every gram of beads. This is calculated assuming complete conversion of the benzyl chloride repeat units to quaternary ammoniums and the mass fractions of the cross-linked styrenic domain and the functional domain. A MO solution (15 mL) containing 15.0 mg of MO dye was added to a vial containing 12.3 mg of PIMS11-HQ. The solution was given 18 h to equilibrate to ensure maximum uptake of the dye before measurement. 29.3% of the dye was absorbed according to UV−vis measurements, meaning that 358 mg of the dye was absorbed per gram of PIMS-11HQ. This is 60% of the expected value based on the stoichiometry of the bead assuming 100% conversion to the quaternary ammonium chloride salt. The reduced capacity compared to the expected value could be attributed to hydrolysis of the benzyl chloride group to benzyl alcohol. Under identical conditions, the HPR4811 Amberlite resin absorbed 55 mg of dye per gram of resin. Therefore, the PIMS-11HQ beads showed fast dye sorption kinetics and a high capacity for dye relative to commercial resins.

CONCLUSIONS

We report the preparation of mesoporous polymer particles from suspension polymerization by means of the PIMS process. We observed spherical particle formation despite the presence of a macromolecular porogen that increased the viscosity of the pre-polymer solution. The bead microstructure was controlled by the PCL-PSDVB diblock microphase separation within each polymer bead. The percolating structure could be etched with alkaline solutions to yield pore size distributions in the mesopore range that could be tuned by selection of the starting PCL macroCTA molar mass. Particle size could be independently tuned by adjusting the stir rate during polymerization. Other factors such as the divinylbenzene fraction in the feed and stabilizer concentration had little effect on the particle size or microstructure. Beads with average particle diameters from 67 to 370 μm were prepared with up to a 82% yield on 20 g scales.

Beads bearing cationic or anionic polymer blocks confined to nanoscale channels were also prepared. These were prepared similarly to the neutral beads but utilized a diblock macroCTA. In the resulting beads, the midblock between the PCL and the cross-linked PS was either PVBC or PTBA, which could be functionalized into a quaternary ammonium cation or an acrylic acid anion, respectively. These functional beads

https://doi.org/10.1021/acsapm.2c00210
ACS Appl. Polym. Mater. 2022, 4, 4219−4233

exhibited a high capacity for dye (360 mg/g bead) and a rate constant of dye sorption of 0.036 s^{-1} in the presence of excess dye. This rate is approximately 250 times greater than a commercial ion-exchange resin using equivalent masses of Amberlite resin and the prepared cationic beads. Owing to the tunability of the polymer framework, we expect that this system could be used to enable the introduction of a variety of targeted functional groups for chemical uptake and/or heterogeneous catalysis.

■ ASSOCIATED CONTENT

Supporting Information

The Supporting Information is available free of charge at https://pubs.acs.org/doi/10.1021/acsapm.2c00210.

Additional characterization data of PCL macroCTAs and beads (NMR, SEC, DSC, TGA, IR, nitrogen sorption isotherms, Raman microscopy spectra, and image analysis), additional optical and scanning electron microscope images, combustion elemental analysis, and additional information on etching conditions (PDF)

■ AUTHOR INFORMATION

Corresponding Author

Marc A. Hillmyer − *Department of Chemistry, University of Minnesota, Minneapolis, Minnesota 55455-0431, United States;* orcid.org/0000-0001-8255-3853; Email: hillmyer@umn.edu

Authors

Colin H. Peterson − *Department of Chemistry, University of Minnesota, Minneapolis, Minnesota 55455-0431, United States*

Jay R. Werber − *Department of Chemistry, University of Minnesota, Minneapolis, Minnesota 55455-0431, United States;* orcid.org/0000-0002-6551-5983

Hyung Kae Lee − *Department of Chemistry, University of Minnesota, Minneapolis, Minnesota 55455-0431, United States*

Complete contact information is available at: https://pubs.acs.org/10.1021/acsapm.2c00210

Notes

The authors declare no competing financial interest.

■ ACKNOWLEDGMENTS

This material is based upon work supported by the U.S. Department of Energy, Office of Science, Office of Basic Energy Sciences under Award Number DE-SC0020210. We thank Bing Luo for assistance with Raman microscopy and Fang Zhou for the preparation of microtome samples. We also acknowledge the Research Analytical Laboratory of the Department of Soil, Water, and Climate for the performance of combustion analysis. Parts of this work were carried out in the Characterization Facility, University of Minnesota, which receives partial support from the NSF through the MRSEC program. This work benefited from the use of the SasView application, originally developed under the NSF award DMR-0520547. SasView contains code developed with funding from the European Union's Horizon 2020 research and innovation program under the SINE2020 project, grant agreement no 654000.

■ REFERENCES

(1) Kawaguchi, H. Functional polymer microspheres. *Prog. Polym. Sci.* **2000**, *25*, 1171−1210.

(2) Gokmen, M. T.; Du Prez, F. E. Porous polymer particles-A comprehensive guide to synthesis, characterization, functionalization and applications. *Prog. Polym. Sci.* **2012**, *37*, 365−405.

(3) Ramli, R. A. Hollow polymer particles: a review. *RSC Adv.* **2017**, *7*, 52632−52650.

(4) Zhang, X.; Zhao, Y.; Xu, S.; Yang, Y.; Liu, J.; Wei, Y.; Yang, Q. Polystyrene sulphonic acid resin with enhanced acid strength via macromolecular self-assembly within confined nanospace. *Nat. Commun.* **2014**, *5*, 3170.

(5) Boysen, R. I. Advances in the development of molecularly imprinted polymers for the separation and analysis of proteins with liquid chromatography. *J. Sep. Sci.* **2019**, *42*, 51−71.

(6) Arcos-Casarrubias, J. A.; Cruz-Díaz, M. R.; Cardoso-Martínez, J.; Vázquez-Arenas, J.; Caballero-Domínguez, F. V. Chromium adsorption into a macroporous resin based on vinylpyridine-divinylbenzene copolymers: thermodynamics, kinetics, and process dynamic in a fixed bed column. *Adsorption* **2018**, *24*, 105−120.

(7) Han, S.; Zang, Y.; Gao, Y.; Yue, Q.; Zhang, P.; Kong, W.; Jin, B.; Xu, X.; Gao, B. Co-monomer polymer anion exchange resin for removing Cr(VI) contaminants: Adsorption kinetics, mechanism and performance. *Sci. Total Environ.* **2020**, *709*, 136002−136011.

(8) Simoes-Cardoso, J. C.; Yoshimoto, N.; Yamamoto, S. Thermodynamic analysis of polyphenols retention in polymer resin chromatography by van't Hoff plot and isothermal titration calorimetry. *J. Chromatogr. A* **2019**, *1608*, 460405.

(9) Okay, O. Macroporous copolymer networks. *Prog. Polym. Sci.* **2000**, *25*, 711−779.

(10) Macintyre, F. S.; Sherrington, D. C. Control of Porous Morphology in Suspension Polymerized Poly(divinylbenzene) Resins Using Oligomeric Porogens. *Macromolecules* **2004**, *37*, 7628−7636.

(11) Smigol, V.; Svec, F. Synthesis and Properties of Uniform Beads Based on Macropoorous Copolymer Glycidyl Methacrylate-Ethylene Dimethacrylate: A Way to Improve Separation Media for HPLC. *J. Appl. Polym. Sci.* **1992**, *46*, 1439−1448.

(12) Jacobelli, H.; Bartholin, M.; Guyot, A. Styrene-Divinylbenzene Copolymers II. Influence of the Nature of the Diluent on the Texture of Macroporous Copolymers. *Angew. Makromol. Chem.* **1979**, *80*, 31−51.

(13) Garcia-Diego, C.; Cuellar, J. Synthesis of Macroporous Poly(styrene-*co*-divinylbenzene) Microparticles Using *n*-heptane as the porogen: Quantitative Effects of the DVB Concentration and the Monomeric Fraction on their Structural Characteristics. *Ind. Eng. Chem. Res.* **2005**, *44*, 8237−8247.

(14) Pastukhov, A. Mesoporous polymer systems based on divinylbenzene copolymers modified with linear rubbers. *Eur. Polym. J.* **2020**, *124*, 109480.

(15) Malik, D. J.; Webb, C.; Holdich, R. G.; Ramsden, J. J.; Warwick, G. L.; Roche, I.; Williams, D. J.; Trochimczuk, A. W.; Dale, J. A.; Hoenich, N. A. Synthesis and characterization of size-selective nanoporous polymeric adsorbents for blood purification. *Sep. Purif. Technol.* **2009**, *66*, 578−585.

(16) Bates, F. S.; Fredrickson, G. H. Block Copolymers-Designer Soft Materials. *Phys. Today* **1999**, *52*, 32−38.

(17) Zalusky, A. S.; Olayo-Valles, R.; Taylor, C. J.; Hillmyer, M. A. Mesoporous Polystyrene Monoliths. *J. Am. Chem. Soc.* **2001**, *123*, 1519−1520.

(18) Lee, J. S.; Hirao, A.; Nakahama, S. Polymerization of Monomers Containing Functional Silyl Groups. 5. Synthesis of New Porous Membranes with Functional Groups. *Macromolecules* **1988**, *21*, 274−276.

(19) Thurn-Albrecht, T.; Steiner, R.; DeRouchey, J.; Stafford, C. M.; Huang, E.; Bal, M.; Tuominen, M.; Hawker, C. J.; Russell, T. P. Nanoscopic Templates from Oriented Block Copolymer Films. *Adv. Mater.* **2000**, *12*, 787−791.

(20) Hampu, N.; Werber, J. R.; Chan, W. Y.; Feinberg, E. C.; Hillmyer, M. A. Next-Generation Ultrafiltration Membranes Enabled by Block Polymers. *ACS Nano* **2020**, *14*, 16446−16471.
(21) Carvalho, B. L.; Lescanec, R. L.; Thomas, E. L. Grain Boundary Defects in Block Copolymer Systems: Bulk and Thin Film Results. *Macromol. Symp.* **1995**, *98*, 1131−1146.
(22) Winter, H. H.; Scott, D. B.; Gronski, W.; Okamoto, S.; Hashimoto, T. Ordering by Flow near the Disorder-Order Transition of a Triblock Copolymer Styrene-Isoprene-Styrene. *Macromolecules* **1993**, *26*, 7236−7244.
(23) Bates, F. S. Network Phases in Block Copolymer Melts. *MRS Bull.* **2005**, *30*, 525−532.
(24) Ha, S.; La, Y.; Kim, K. T. Polymer Cubosomes: Infinite Cubic Mazes and Possibilities. *Acc. Chem. Res.* **2020**, *53*, 620−631.
(25) Charleux, B.; Delaittre, G.; Rieger, J.; D'Agosto, F. Polymerization-Induced Self-Assembly: From Soluble Macromolecules to Block Copolymer Nano-Objects in One Step. *Macromolecules* **2012**, *45*, 6753−6765.
(26) Warren, N. J.; Armes, S. P. Polymerization-Induced Self-Assembly of Block Copolymer Nano-Objects via RAFT Aqueous Dispersion Polymerization. *J. Am. Chem. Soc.* **2014**, *136*, 10174−10185.
(27) Penfold, N. J. W.; Yeow, J.; Boyer, C.; Armes, S. P. Emerging Trends in Polymerization-Induced Self-Assembly. *ACS Macro Lett.* **2019**, *8*, 1029−1054.
(28) Liu, C.; Hong, C.-Y.; Pan, C.-Y. Polymerization Techniques in Polymerization-Induced Self-Assembly (PISA). *Polym. Chem.* **2020**, *11*, 3673−3689.
(29) Kwon, J. H.; Kim, J.; Kim, K. T. Photo-crosslinked polymer cubosomes as a recyclable nanoreactor in organic solvents. *Polym. Chem.* **2021**, *12*, 2701−2711.
(30) Seo, M.; Hillmyer, M. A. Reticulated Nanoporous Polymers by Controlled Polymerization-Induced Microphase Separation. *Science* **2012**, *336*, 1422−1425.
(31) Vidil, T.; Hampu, N.; Hillmyer, M. A. Nanoporous Thermosets with Percolating Pores from Block Polymers Chemically Fixed above the Order-Disorder Transition. *ACS Cent. Sci.* **2017**, *3*, 1114−1120.
(32) Bates, F. S.; Rosedale, J. H.; Fredrickson, G. H. Fluctuation effects in a symmetric diblock copolymer near the order-disorder transition. *J. Chem. Phys.* **1990**, *92*, 6255−6270.
(33) Schulze, M. W.; Hillmyer, M. A. Tuning Mesoporosity in Cross-Linked Nanostructured Thermosets via Polymerization-Induced Microphase Separation. *Macromolecules* **2017**, *50*, 997−1007.
(34) Chopade, S. A.; So, S.; Hillmyer, M. A.; Lodge, T. P. Anhydrous Proton Conducting Polymer Electrolyte Membranes via Polymerization-Induced Microphase Separation. *ACS Appl. Mater. Interfaces* **2016**, *8*, 6200−6210.
(35) Oh, J.; Kim, B.; Lee, S.; Kim, S.-H.; Seo, M. Semipermeable Microcapsules with a Block-Polymer-Templated Nanoporous Membrane. *Chem. Mater.* **2018**, *30*, 273−279.
(36) Werner, J. G.; Lee, H.; Wiesner, U.; Weitz, D. A. Ordered Mesoporous Microcapsules from Double Emulsion Confined Block Copolymer Self-Assembly. *ACS Nano* **2021**, *15*, 3490−3499.
(37) Li, X.; Zhang, Q.; Li, Z.; Xu, S.; Zhao, C.; Chen, C.; Zhi, X.; Wang, H.; Zhu, N.; Guo, K. Tripodal hydrogen bond donor binding with sulfonic acid enables ring-opening polymerization. *Polym. Chem.* **2016**, *7*, 1368−1374.
(38) Zhou, X.; Hong, L. Controlled ring-opening polymerization of cyclic esters with phosphoric acid as catalysts. *Colloid Polym. Sci.* **2013**, *291*, 2155−2162.
(39) Lai, J. T.; Filla, D.; Shea, R. Functional Polymers from Novel Carboxyl-Terminated Trithiocarbonates as Highly Efficient RAFT Agents. *Macromolecules* **2002**, *35*, 6754−6756.
(40) Dong, X. H.; Obermeyer, A. C.; Olsen, B. D. Three-Dimensional Ordered Antibody Arrays Through Self-Assembly of Antibody-Polymer Conjugates. *Angew. Chem., Int. Ed.* **2017**, *56*, 1273−1277.
(41) Makiguchi, K.; Satoh, T.; Kakuchi, T. Diphenyl Phosphate as an Efficient Cationic Organocatalyst for Controlled/Living Ring-Opening Polymerization of δ-Valerolactone and ε-Caprolactone. *Macromolecules* **2011**, *44*, 1999−2005.
(42) Horák, D.; Labský, J.; Pilař, J.; Bleha, M.; Pelzbauer, Z.; Švec, F. The effect of polymeric porogen on the properties of macroporous poly(glycidyl methacrylate-co-ethylene dimethacrylate). *Polymer* **1993**, *34*, 3481−3489.
(43) Ferreira, A.; Bigan, M.; Blondeau, D. Optimization of a polymeric HPLC phase: poly(glycidyl methacrylate-co-ethylene dimethacrylate). *React. Funct. Polym.* **2003**, *56*, 123−136.
(44) Saba, S. A.; Lee, B.; Hillmyer, M. A. Tricontinuous Nanostructured Polymers via Polymerization-Induced Microphase Separation. *ACS Macro Lett.* **2017**, *6*, 1232−1236.
(45) Labet, M.; Thielemans, W. Synthesis of polycaprolactone: a review. *Chem. Soc. Rev.* **2009**, *38*, 3484−3504.
(46) Nakagawa, S.; Tanaka, T.; Ishizone, T.; Nojima, S.; Kamimura, K.; Yamaguchi, K.; Nakahama, S. Crystallization behavior of poly(ε-caprolactone) chains confined in lamellar nanodomains. *Polymer* **2014**, *55*, 4394−4400.
(47) Nakagawa, S.; Ishizone, T.; Nojima, S.; Kamimura, K.; Yamaguchi, K.; Nakahama, S. Effects of Chain-Ends Tethering on the Crystallization Behavior of Poly(ε-caprolactone) Confined in Lamellar Nanodomains. *Macromolecules* **2015**, *48*, 7138−7145.
(48) Porod, G. Die Röntgenkleinwinkelstreuung von dichtgepackten kolloiden Systemen. *Kolloid Z.* **1951**, *124*, 83−114.
(49) Debye, P.; Anderson, H. R.; Brumberger, H. Scattering by an Inhomogeneous Solid. II. The Correlation Function and Its Application. *J. Appl. Phys.* **1957**, *28*, 679−683.
(50) Wong, P.-z. Scattering by inhomogeneous systems with rough internal surfaces: Porous solids and random-field Ising systems. *Phys. Rev. B* **1985**, *32*, 7417−7424.
(51) Sinha, S. K.; Sirota, E. B.; Garoff, S.; Stanley, H. B. X-ray and neutron scattering from rough surfaces. *Phys. Rev. B* **1988**, *38*, 2297−2311.
(52) Avnir, D.; Farin, D.; Pfeifer, P. Molecular fractal surfaces. *Nature* **1984**, *308*, 261−263.
(53) Koga, T.; Kawasaki, K.; Takenaka, M.; Hashimoto, T. Late stage spinodal decomposition in binary fluids: comparison between computer simulation and experimental results. *Physica A* **1993**, *198*, 473−492.
(54) Thommes, M.; Kaneko, K.; Neimark, A. V.; Olivier, J. P.; Rodriguez-Reinoso, F.; Rouquerol, J.; Sing, K. S. W. Physisorption of gases, with special reference to the evaluation of surface area and pore size distribution (IUPAC Technical Report). *Pure Appl. Chem.* **2015**, *87*, 1051−1069.
(55) Hopff, V. H.; Lussi, H.; Gerspacher, P. Zur Kenntnis der Perlpolymerisation. *Die Makromolekulare Chem. Macromol. Chem. Phys.* **1964**, *78*, 37−46.
(56) Hinze, J. O. Fundamentals of the Hydrodynamic Mechanism of Splitting in Dispersion Processes. *AIChE J.* **1955**, *1*, 289−295.
(57) Chaudhary, V.; Sharma, S. Effect of various synthesis parameters on styrene-divinylbenzene copolymer properties. *J. Porous Mater.* **2019**, *26*, 1559−1571.
(58) Dowding, P. J.; Goodwin, J. W.; Vincent, B. Factors governing emulsion droplet and solid particle size measurements performed using the focused beam reflectance technique. *Colloids Surf., A* **2001**, *192*, 5−13.
(59) 100-42-5. Viscosity of Liquids as a Function of Temperature. In *CRC Handbook of Chemistry and Physics [Online]*, 102 ed.; Rumble, J. R., Ed.; CRC Press, 2021. http://hbcponline.com/ ((accessed March 10, 2021).
(60) Saba, S. A. Tunable Morphology of Porous Polymers via Polymerization-Induced Microphase Separation, Ph.D. Dissertation, University of Minnesota: Minneapolis, MN, 2017.
(61) Goldfeld, D. J.; Silver, E. S.; Radlauer, M. R.; Hillmyer, M. A. Synthesis and Self-Assembly of Block Polyelectrolyte Membranes through a Mild, 2-in-1 Postpolymerization Treatment. *ACS Appl. Polym. Mater.* **2020**, *2*, 817−825.
(62) Filippov, A. D.; van Hees, I. A.; Fokkink, R.; Voets, I. K.; Kamperman, M. Rapid and Quantitative De-tert-butylation for

Poly(acrylic acid) Block Copolymers and Influence on Relaxation of Thermoassociated Transient Networks. *Macromolecules* **2018**, *51*, 8316−8323.
(63) Qin, J.; Chen, Y.; Yan, D.; Xi, F. Dispersible Shaped Nanoobjects from Bulk Microphase Separation of High Tg Block Copolymers without Chemical Cross-linking. *Macromolecules* **2010**, *43*, 10652−10658.

https://doi.org/10.1021/acsapm.2c00210
ACS Appl. Polym. Mater. 2022, 4, 4219−4233